

ULRR

A nonlinear and asymmetric monostable compliant ortho-planar spring piezoelectric vibrational energy harvester using a H-I structure

Item Type	Article
Authors	Taufan, Ibnu;Punch, Jeff;Nico, Valeria
Citation	Sensors and Actuators A: Physical, 2024, 379, 115984
Publisher	Elsevier
Rights	Attribution-NonCommercial-ShareAlike 4.0 International
Download date	2026-06-18 17:30:48
Item License	https://creativecommons.org/licenses/by-nc-sa/4.0/
Link to Item	https://hdl.handle.net/10344/15596

A nonlinear and asymmetric monostable compliant ortho-planar spring piezoelectric vibrational energy harvester using a H-I structure

Ibnu Taufan^{a*}, Jeff Punch^a, Valeria Nico^a

^aCONNECT, Stokes Laboratories, Bernal Institute, University of Limerick, Limerick, Ireland

Abstract

This paper proposes a compliant ortho-planar spring piezoelectric vibrational energy harvester (COPS-PVEH) using a H-I structure that exploits a nonlinearity and an asymmetric mono-stability to enhance the bandwidth of the device. The main structure is based on a double clamped beam (I-structure) coupled with four cantilever beams (H-structure) and an ortho-planar spring in the centre of the I-structure. Finite element analysis (FEA), analytical modelling, and experimentation were performed to analyse the dynamical and electrical behaviour of the harvester. The device was fabricated using polylactide (PLA). Six bimorph PZT-5H piezoelectric materials, electrically connected in parallel, were used as piezoelectric generators. The device was tested using an optimum load resistor of 90 k Ω under sinusoidal and sine sweep excitation in the gravity (vertical) direction. The pre-load (due to gravitation) causes a softening nonlinearity and an asymmetric mono-stability in the potential energy function. The results show that multiple peaks are observed in the output voltage of the harvester in the FEA, analytical modelling, and experimentation under harmonic excitation in the sub 15 Hz frequency range. Furthermore, analytical modelling and experimentation exhibit softening nonlinearity and chaotic behaviour, reaching a maximum amplitude power of 1.01 mW (at 8.3 Hz) and 1.07 mW (at 9.5 Hz) respectively under sine sweep excitation (amplitude of 0.6 g ($g = 9.81 \text{ m/s}^2$)). Experimentally, the harvester also generates an average power greater than 46 μW with a 6.8 Hz bandwidth under the same excitation. The softening nonlinearity and asymmetric mono-stability enhance the bandwidth of the harvester in the low frequency region where most broadband ambient vibrations are available in practical environments.

Keywords: Piezoelectric vibrational energy harvesting, ortho-planar spring, softening nonlinearity, asymmetric mono-stability, low frequency, H-I structure

1. Introduction

In the last decade, the number of Wireless Sensor Networks (WSNs) has increased significantly for healthcare, utilities, and transport applications [1]. Most of these sensors are powered by batteries which not only contain material that is harmful to the environment if not correctly disposed of, but also require regular maintenance [2]. When there are thousands of sensors, the regular replacement of traditional batteries becomes impractical and problematic [3]. The application of WSNs in remote locations that are difficult to access also results in high-cost maintenance [4]. The rapid technological development of the WSNs, which only require low power, has attracted great attention from researchers to find sustainable sources to power these sensors from ambient energy [5]. Among other ambient energy sources, mechanical energy is promising because of its abundance in many environments. In particular, piezoelectric vibrational energy harvesters (PVEHs) can convert mechanical energy to electrical energy and represent an alternative solution for batteries because

PVEHs are renewable, reliable, and do not require human intervention [6].

Most PVEHs employ cantilever beam structures to convert strain into electricity. The cantilever beam is generally chosen because of its simple geometric structure and high efficiency of energy conversion [7,8]. However, the drawbacks of this type of harvester are a single resonant mode and narrow frequency bandwidth that are not suitable for broadband ambient vibrations. Therefore, the harvester needs to be tuned to the main frequency of the vibration source, otherwise the harvester's efficiency will be very low [9]. To overcome the problems of single mode and narrow bandwidth, several methods have been proposed in the literature to increase the bandwidth through pure geometrical nonlinearity [10–12], magnetic coupling [13–18], multiple resonators [19,20], bi-stability [21–25], and asymmetric mono and bi-stability [26–28].

Researchers have investigated the benefits of ortho-planar springs in vibrational energy harvesters (VEHs) to induce nonlinearity and multi resonance due to their compactness and ease of production [11,12,29–31]. Mallick *et al.* [30] compared linear and nonlinear stretching in an electromagnetic VEH that featured four linear arms and a nonlinear ortho-planar spring. The

*Corresponding author.

E-mail address: ibnu.taufan@ul.ie (Taufan).

stretching and bending of the nonlinear spring gave a wider half-power bandwidth of 10 Hz under an acceleration amplitude of 1 g, compared to the linear counterpart. Dhote *et al.* [12] compared and analysed three PVEHs using nonlinear compliant ortho-planar springs. The designs exhibited three or more vibration modes below 150 Hz. The addition of proof masses brought the vibration resonances of the harvester closer, and this helped to widen the operational bandwidth. Due to the hardening effect, the design showed the largest frequency bandwidth of 35 Hz and a maximum output voltage of 4 V (peak-to-peak) under forward frequency-sweep excitation at an acceleration amplitude of 0.8 g. Mohammadi *et al.* [31] employed an asymmetric quad leg ortho-planar spring PVEH with an S-shape structure to increase the harvester's bandwidth. The experimental results showed that the asymmetries contributed to an increase in the bandwidth of the harvester compared to a symmetrical design.

H-shape and double clamped beam (I-shape) structures based piezoelectric and electromagnetic VEHs also exhibited multi-modal and nonlinear frequency responses [20,32–36], providing broad bandwidth. Liang *et al.* [20] and Gafforelli *et al.* [32] studied a double clamped beam (I-shape) PVEH which could increase the bandwidth of the harvester. The beam bended and stretched during the oscillation, leading to tensional stress along the beam. Consequently, a hardening nonlinearity was observed, and this enhanced the bandwidth of the harvester. Wang *et al.* [34] investigated a H-shaped PVEH which comprised a main beam and two sub-beams with tip masses for engine fault monitoring purposes. The device could harvest vibrations in two directions (vertical and horizontal axes) effectively. The output voltage from the main beam was 1.011 V at 110 Hz, and the output voltage from the sub-beams was 1.021 V at 118 Hz, respectively, under an acceleration amplitude of 0.35 g. Toyabur *et al.* [35] proposed a multi-modal PVEH based on a main double clamped beam coupled with four cantilever beams for low frequency vibrations. Four tip masses and four piezoelectric layers were employed on the four cantilever beams. The harvester showed four peaks of output power between 8 Hz and 22 Hz, gaining a maximum power 740 μ W under 0.4 g. Sun *et al.* [36] developed a three-dimensional structure PVEH that exhibited multi-resonances between 20 Hz and 100 Hz, which was able to harvest vibrations in three axes equally. The harvester consisted of a buckled ribbon with optional Kirigami cuts. The buckled ribbon was a double clamped beam, mechanically coupled with four cantilever beams without proof masses. The harvester exhibited three main peaks between 15 Hz and 100 Hz and could harvest a maximum output voltage of 15 mV amplitude under 2.2 m/s wind speed in a vertical direction.

Bistable PVEHs have been studied to increase the bandwidth of the harvester because they exhibit three behaviours; intra-well, chaotic, and inter-well [20,37]. The bistable VEH has been proven to have a wider bandwidth compared to linear (monostable) counterparts [38,39]. Hou *et al.* [24] introduced a bistable origami PVEH for scavenging human shaking energy. The harvester had a pedestal, two piezoelectric materials, two hinges, two connecting rods, a slide rail, a linear bearing, a slider, and an end cap. The two stable states occurred when the slider snapped through from below to above the initial state, causing chaotic behaviour in an unstable region. The harvester generated a maximum output power of 2.2 mW at 6.2 Hz under 1.2 g excitation. One of the disadvantages of such a design is that it requires a complex assembly. Furthermore, the bistable PVEHs also required a large excitation in order to overcome the potential barrier to activate the chaotic or inter-well behaviour [40]. Another drawback was that the bistability induced larger strain levels, leading to shorter lifetime of the harvester [28].

To solve these problems, an asymmetric monostable potential function has been introduced to eliminate the potential barrier and lower the strain of the harvester. Kumar *et al.* [28] experimentally proved that the asymmetric monostable harvester exhibited an improvement in the output power compared to the symmetric monostable (linear) and bistable configurations. The harvester consisted of a cantilever beam with a magnet on its free end and a cylindrical magnet below the vertical clamped position to introduce asymmetric monostable and symmetric bistable configurations. The result showed that the proposed asymmetric monostable harvester combined the benefit of both linear and bistable configurations by gaining a high-power output while producing lower strain levels under the same excitation level. However, a drawback of the magnetic-based asymmetric monostable PVEH was that it could interact with sensors to be powered [41].

Previously reported papers revealed that VEHs only exhibit multi-modal behaviour and the hardening nonlinearity at frequencies higher than 15 Hz. However, a disadvantage of the hardening nonlinearity is that high external excitation is required to induce the nonlinear effect. However, even if the asymmetric mono-stability, achieved using magnets, has been shown to be an effective way to improve the performance and lifetime of the PVEH compared to linear and bistable harvesters, magnetic-based asymmetric mono-stability is not ideal for practical applications.

In this paper, a softening nonlinear and asymmetric monostable PVEH, based on magnet-free, non-complex assembly, and a simple double clamped beam is proposed. The proposed harvester features a H-I structure and an ortho-planar spring. The softening nonlinearity and asymmetric mono-stability, due to a pre-load (gravitational effect), are employed to enhance the performance and bandwidth of the device at relatively low frequencies (below 15 Hz) and at low levels of excitation (amplitudes below 0.6 g) in the vertical direction. The harvester is the combination of a main double clamped beam (I-structure), four cantilever beams (H-structure) and a four-arm ortho-planar spring [30] at the centre of the main structure. A proof centre mass and four tip masses are added on the spring and tip arms respectively to induce high strains in the structure.

Initially, modal analysis (natural frequency) of the harvester design is conducted through finite element analysis (FEA). Then, mechanical (natural frequency) and electrical characteristics of the harvester under sinusoidal excitation are evaluated analytically (linear), numerically (linear), and experimentally. Two resonance frequencies appear on both displacement and voltage responses in all analyses between 6 Hz and 15 Hz. An additional two peaks can also be seen due to multi-directional behaviour, and chaotic behaviour which improve the performance under harmonic excitation. Then, analytical modelling using a nonlinear six degree of freedoms (DOFs) harmonic oscillator and experimentation are conducted to analyse the mechanical and electrical behaviour of the harvester under sine sweep excitation to verify its nonlinear and asymmetric mono-stable behaviour. Finally, the results are compared with previous PVEHs in the low frequency region using normalised power density (NPD). A softening nonlinearity and asymmetric mono-stability (chaotic behaviour) are observed in both the nonlinear six DOFs and experimentation, which improve the performance and bandwidth of the harvester. To the authors' knowledge, this paper is one of the first works which introduces the multi-modal, softening nonlinear, and chaotic behaviour (due to an asymmetric monostable potential) in a PVEH by employing a simple and planar structure without using any magnets. All the characteristics aim to enhance the performance and bandwidth as well as lowering the strain on the structure leading to an improvement of the lifetime of the harvester.

2. Design and operating principle

In this section, the design and operating principle of the harvester are described. The structure has an overall dimension of 196 mm length, 60 mm width, and 1 mm thickness. The dimension was selected so that the harvester has the first two natural frequencies in vertical axis below 15 Hz. The structure was made of polylactide (PLA) which was fabricated using 3D printing techniques. The structure consists of one double clamped beam (main beam) as an I-structure, four cantilever beams (arms) as a H-structure, and an ortho-planar spring, as shown in Fig. 1. The main beam is fixed on both sides, and the four arms are free to oscillate. The ortho-planar spring, which is also free to oscillate in the centre of the main beam, is intended to provide additional modes to the structure in the low frequency range (<15 Hz), hence increasing the bandwidth of the harvester [42].

Fig. 2 presents the dimensions of the harvester in detail. Fig. 2 (b) shows the side view of the harvester (all planar) before gravitational pre-loading. After pre-load, the H structure and the ortho-planar spring are planar, while the I-structure (see the red dashed lines in Fig. 2 (a)) has a 5 mm pre-load relative to the planar parts due to gravitation (in Figure 2 (c)). To induce high strain on the structure, a 20-grammes proof mass and four 3-grammes tip masses (made of tungsten putty) are added on the ortho-planar spring and tip arms respectively. The proof mass on ortho-planar spring (20-grammes) has to be higher than the total of the proof masses on the tip mass (12-grammes) to achieve the highest deflection in the first mode shape on the ortho-planar spring which is similar to the first mode shape of the conventional double clamped beam.

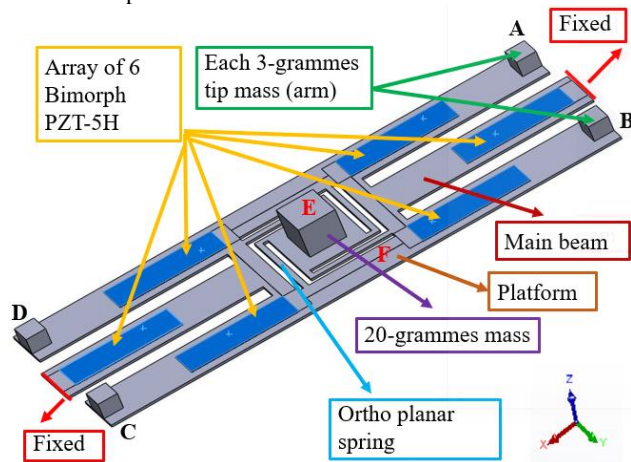


Fig. 1. Schematic of the harvester.

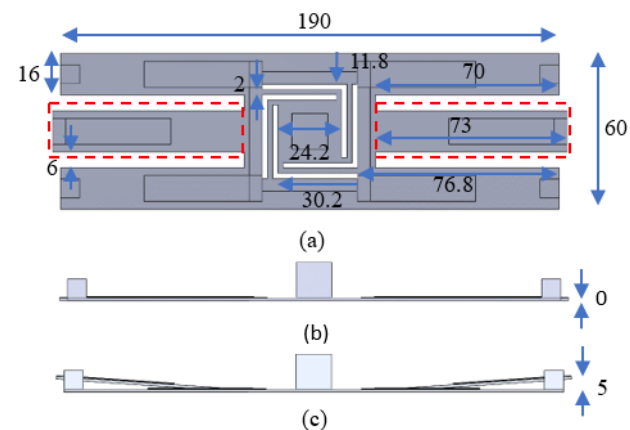


Fig. 2. The dimension of the harvester: (a) top view; (b) side view (planar); (c) side view (after pre-load). Dimensions are in mm.

The harvester is designed to convert mechanical energy (vibration) in the vertical (z) axis. When there is an external excitation along the z axis (see the cartesian coordinate system in Fig. 1), the end of the four arms (tip arm) with four tip masses, the ortho-planar spring with the proof mass, and the middle of the main beam (platform) oscillate, creating maximum strain in six locations where six bimorph PZT-5H piezoelectric materials are attached.

The basic working principle of the harvester is similar to a conventional single cantilever beam where one side is clamped and the other side is free to oscillate, resulting in strain near the clamped area. The middle of the main beam (I-structure), platform (F), ortho-planar spring and 20-grammes proof mass (E), and tip masses on the four cantilever beams (A, B, C, and D) in Fig. 1 are free to oscillate, creating high strain in the six locations near the clamped area.

The bimorph PZT-5H materials then convert the strain into useful electricity. The bimorph PZT-5H material (Steminc, part number SMBA4510T05M) is 40 mm long, 10 mm wide, and 0.2 mm thick. The dimension of the copper substrate of the bimorph PZT-5H, is 45 mm x 10 mm x 0.1 mm. Table 1 lists the material parameters of PZT-5H, copper, PLA, and tungsten putty for FEA, modelling and experimentation.

Table 1. Material parameters.

Parameters	Value
PZT-5H Material (Steminc)	
Density	7900 kg/m ³
Young's modulus	72 GPa
Poisson's ratio	0.3
Piezo constant (d_{31})	270e-12 m/V
Electrical permittivity ϵ	3500 ϵ_0 (F/m)
Damping loss factor	0.1
Copper [43]	
Density	8900 kg/m ³
Young's modulus	11 GPa
Poisson's ratio	0.35
Loss factor	0.1
PLA [44–46]	
Density	1250 kg/m ³
Young's modulus (planar)	1.92 GPa
Young's modulus (pre-load)	1.68 GPa
Poisson's ratio	0.36
Loss factor	0.1
Tungsten Putty	
Density	7800 kg/m ³
Young's modulus	193 GPa
Poisson's ratio	0.33

3. Methodology

In this section, the methodology for the FEA procedure, analytical modelling, and experimental setup are presented. Material properties, simulation procedure, boundary conditions, and an equivalent circuit are described in subsection 3.1. The linear and nonlinear six DOFs modelling are detailed in subsection 3.2, and the experimental set up, the harvester, and the experimental procedure are reported in subsection 3.3.

3.1. FEA procedure

FEA was carried out using COMSOL Multiphysics 6.0 to understand the mechanical and electrical behaviour of the harvester. Both sides of the double clamped beam were

considered to be fixed, as shown in Fig. 1. The structure is made of polylactide (PLA). The 20-grammes and 3-grammes proof masses were modelled as tungsten putty cubes of side 13.68 mm and 7.27 mm respectively. Properties of the materials are listed in Table 1. Physics-controlled and normal size mesh were selected, and the convergence error was set to 0.0002. Initially, static analysis in the solid mechanics module was used to analyse the force-displacement curve and the potential energy of the harvester using linear and nonlinear analysis.

To analyse the mechanical (mode shape) and electrical behaviour of the harvester, solid mechanics, electrostatics, and electrical circuit in the microelectromechanical systems (MEMS) module [42,47] were coupled in COMSOL Multiphysics using linear analysis. The proposed FEA model has been validated against literature in a previous work of the group [42]. Harmonic 0.2 g, 0.4 g, and 0.6 g (amplitude) external accelerations along the z axis were used to calculate the output displacement and voltage. The harmonic acceleration was varied in frequency from 6 Hz to 15 Hz in steps of 0.25 Hz.

The equivalent circuit design of the six PZT-5H generators is represented as a parallel connection in the FEA model, as shown in Fig. 3. Each PZT-5H material was modelled as a voltage source (V_p), an internal piezo-element resistance (R_p), and capacitance (C_p) [48]. The top electrodes were connected to a 90 k Ω (optimum load resistor), while the bottom electrodes were connected to ground, and the voltage across the load resistor was calculated in order to analyse the electrical behaviour of the harvester.

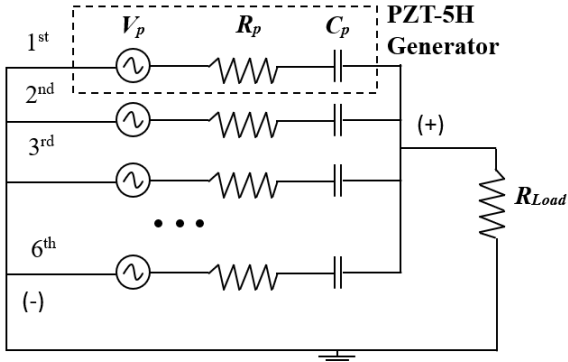


Fig. 3. Equivalent circuit of six PZT-5H generators in a parallel connection.

3.2. Analytical modelling

Two configurations of the harvester were analytically modelled: linear and nonlinear. Under harmonic excitation, the linear six DOFs modelling was employed to estimate the dynamical and electrical behaviour of the harvester in conjunction with the linear FEA model. Then, the nonlinear six DOFs modelling was carried out to analyse the harvester under sine sweep excitations, and these results were compared with experimentation. Fig. 4 shows the equivalent mechanical model of the harvester, which is modelled as six DOFs harmonic oscillator using simplified lumped models that consist of mass, spring, damper, and piezoelectric element. The term of the six DOFs of the harvester comes from the six different masses, such as platform, ortho-planar spring, and four cantilever beams, that have independent coordinates of motions along the z-axis (motion along the x, y, and rotations are not allowed).

The I-structure and the two bimorphs piezoelectric material are modelled as stiffness (k_l) and piezo elements with the base excitation; the platform is modelled as m_1 ; and the ortho-planar spring and 20-grammes mass are modelled as c_2 , k_2 , and m_2 . The

nonlinear softening stiffness (k_s) is considered in the ortho-planar spring for the nonlinear approach, while k_s is ignored for the linear case; the arms (H-shape), 3-grammes mass, and a bimorph piezoelectric material are modelled as c_3 , k_3 , m_3 , and the piezo element for the first arm, and the remaining arms as c_n , k_n , m_n , and the piezoelectric element, where the maximum value of $n = 6$; and the displacement responses of the masses and base excitation are modelled as z .

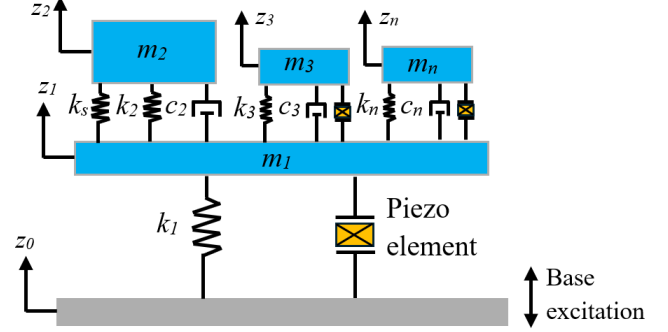


Fig. 4. Equivalent mechanical model of the harvester (the k_s values can be present (nonlinear) or absent (linear)).

The equations of motion, coupled piezo element, conversion coefficient, characteristic cut-off frequency, power equation are presented in the following equations [49,50] (the k_s can be present (nonlinear) or absent (linear)).

The equations of motion:

$$m_1 \ddot{z}_1 + (c_2 + c_3 + c_n) \dot{z}_1 + (k_1 + k_2 + k_3 + k_n) z_1 - k_s z_1^3 = c_2 \dot{z}_2 + k_2 z_2 + c_3 \dot{z}_3 + k_3 z_3 - k_s z_2^3 + c_n \dot{z}_n + k_n z_n - m_1 a - \alpha V_L \quad (1)$$

$$m_2 \ddot{z}_2 + c_2 \dot{z}_2 + k_2 z_2 - k_s z_2^3 = c_2 \dot{z}_1 + k_2 z_1 - k_s z_1^3 - m_2 a \quad (2)$$

$$m_3 \ddot{z}_3 + c_3 \dot{z}_3 + k_3 z_3 = c_3 \dot{z}_1 + k_3 z_1 - \alpha V_L - m_3 a \quad (3)$$

$$m_n \ddot{z}_n + c_n \dot{z}_n + k_n z_n = c_n \dot{z}_1 + k_n z_1 - \alpha V_L - m_n a \quad (4)$$

The coupled piezoelectric equation:

$$\dot{V}_L + \omega_c V_L = \delta_c \omega_c (\dot{z}_1 + \dot{z}_2 + \dot{z}_3 + \dot{z}_n) \quad (5)$$

with

$$\delta_c = \alpha R_L \quad (6)$$

$$\omega_c = 1/(R_L C_0) \quad (7)$$

Where: α is the electromechanical coupling coefficient of the piezoelectric element; V_L is the generated voltage of all piezoelectric elements, which are connected in parallel, across the optimum load (R_L); δ_c (equation 6) is the conversion coefficient; ω_c (eq 7) is the characteristic cut-off frequency; and C_0 is the capacitance. The amplitude power (P) is defined as

$$P = \frac{V_L^2}{R} \quad (8)$$

The linear and nonlinear stiffness were calculated through the FEA study. Details on how the parameters are calculated are provided in section 4.1. Due to simplification of the harvester in the modelling, a correction factor of $1e-4$ was used in the k_s value, so the k_s from the FEA simulation becomes $1.73e4$ N/m³. The parameter k_s was only considered in the analytical modelling to simplify the model and predict the softening nonlinearity of the system in the experimentation. The system of equations was solved via Matlab, using the Runge-Kutta numerical algorithm, to analyse the dynamical and electrical behaviour of the harvester under 0.2 g, 0.4 g, and 0.6 g base excitation. Simulated results will be present in sections 4.3, 4.4, 5.1, and 5.2. Table 2 shows the parameters used for the six DOFs modelling.

Table 2. Parameters of the six DOFs modelling.

Parameter (symbol)	Value
m_1	55 grammes
m_2	22.05 grammes
$m_3 = m_n$	6.78 grammes
k_1	647.49 N/m
k_2	143.82 N/m
$k_3 = k_n$	71.38 N/m
k_s	1.73e8 N/m ³
c_2 (linear)	0.0824 N s/m
c_2 (nonlinear)	0.1648 N s/m
$c_3 = c_n$ (linear)	0.011 N s/m
$c_3 = c_n$ (nonlinear)	0.022 N s/m
α (linear)	2.2e-5 N/V
α (nonlinear)	3.19e-5 N/V
C_0	240 nF
R_L	90 k Ω

3.3. Experimentation

Experimentation was conducted to validate the simulation and modelling results of the harvester. Fig. 5 illustrates the schematic of the experimental setup: the I-beam was clamped on both sides of the main beam to a holder, then fixed on an LDS V406 electromagnetic shaker that acted as a vibration source. A PCB Piezotronics 353B03 accelerometer was mounted on the head of the shaker to provide feedback control in order to set the desired acceleration amplitude level. The positive and negative electrodes of the PZT-5H materials, using a parallel connection, were connected to a resistance decade box set to a value of 90 k Ω (optimum resistor). The displacements of both the tip arm and the centre of the proof mass were measured with two laser displacement sensors: a Panasonic HL-G112-A-C5), and a Micro-Epsilon optoNCDT LD1607-20, respectively. The output voltage was recorded across the load resistance under both harmonic and sine sweep excitation. LabVIEW was used to drive the shaker and to acquire signals from the accelerometer, the laser displacement gauge, and the output voltage of the harvester. Furthermore, the chaotic behaviour was identified using a high-speed camera (Make/Model).

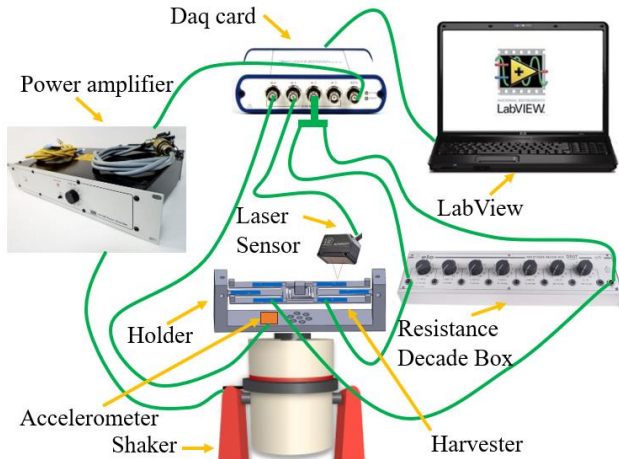
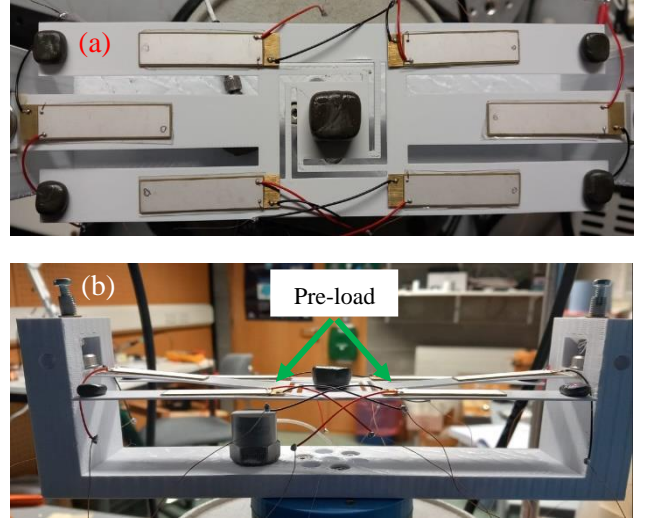
**Fig. 5.** Schematic of the experimental setup.**Fig. 6.** Design of the harvester (a) top view; and (b) side view.

Fig. 6 presents a design of the harvester from both top view and side view. From the side view, the pre-load due to gravitation made the I-beam to buckle down (5 mm) with respect to the planar parts (initial position before pre-load). The proof masses consisted of one 20-grammes and four 3-grammes tungsten putty (Dark matter, weed green). The PZT-5H piezoelectric materials were bonded to the H-I structure using double-sided polyester tape. Harmonic excitations of 0.2 g, 0.4 g, and 0.6 g (amplitude) along the z axis were imposed to measure the displacement of the tip arm and of the proof mass, in order to obtain the natural frequency (mechanical behaviour) of the harvester. Simultaneously, the output voltage was measured to analyse the electrical behaviour. The frequency of the excitation was varied from 6 Hz to 15 Hz in steps of 0.5 Hz. To calculate the relative displacement of both tip arm and proof mass with respect to the shaker head, the measured displacement was reduced by the shaker displacement. Then, the harvester was also tested under forward and backward sweeps (amplitude of 0.2 g, 0.4 g, and 0.6 g) to verify the presence of nonlinear and asymmetric monostable behaviour through the displacement of the tip arm and the output power.

4. The analysis of the harvester using linear FEA, analytical modelling, and experimentation under harmonic excitation

In this section, the static behaviour and potential energy of the harvester was analysed using FEA to understand the displacement response under static force for the buckled-down 5 mm configuration (after pre-load). After that, modal analysis was carried out in FEA to determine the mode shape using a planar approach. Then, mechanical and electrical behaviours of the harvester were studied using linear FEA simulations, linear six DOFs analytical model, and experimentation. In the last subsection, chaotic analysis was also carried out to analyse the chaotic behaviour of the harvester.

4.1. Elastic potential energy using FEA

The elastic potential energy was studied using FEA for the buckled-down 5 mm configuration as the actual experimentation showed a pre-load due to gravitation. In this analysis, the force (F) was imposed on the top of the 20-grammes proof mass, and the displacement response (D) was calculated at the same

location. The force was applied from about -1 N to 1 N, and the displacement was calculated. The analysis was carried out in COMSOL using linear (as reference) and nonlinear analysis.

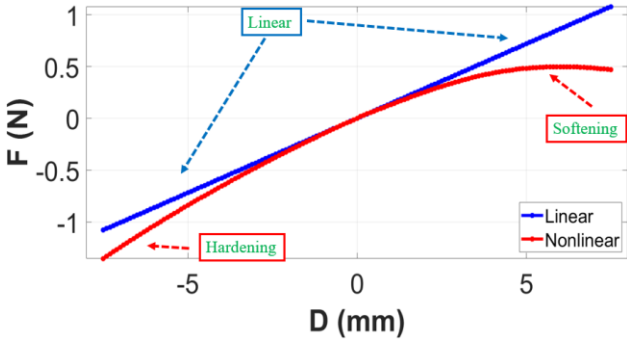


Fig. 7. The force (F)-displacement (D) curve using linear and nonlinear analysis.

The nonlinear force-displacement response in Fig. 7 shows hardening nonlinearity from -7.5 mm to 0 mm due to stretching. Interestingly, the displacement response for forces greater than 0 N exhibits softening nonlinearity, where the displacement is greater compared to the linear response due to softening stiffness. The main source of the softening nonlinearity is caused by the buckled-down 5 mm configuration, and the ortho-planar structure due to the dominant axial (inertial) force [51]. To estimate the asymmetric monostable behaviour of the harvester, the potential energy was calculated considering the softening displacement response only from the static analysis. The total potential energy of the harvester is expressed by [52]:

$$U(z_2) = \frac{1}{4}k_s(z_2)^4 + \frac{1}{2}(-k_2)(z_2)^2 + m_2gz_2 \quad (9)$$

Where k_s (softening stiffness) is $1.73e8 \text{ N/m}^3$, and m_2 is 22.05 grammes. The variables z_2 , k_2 , and $U(z_2)$ represent the displacement on the 20-grammes proof mass, the linear spring stiffness, and the potential energy as a function of the displacement, respectively. The k_s value was calculated through fourth order polynomial fitting in Matlab from the data reported in Fig. 7. Fig. 8 shows the potential energy as a function of the displacement of the 20-grammes proof mass that was calculated in the previous static analysis. The potential energy shows an asymmetric well at a displacement of -0.8 mm. This introduces an asymmetric mono-stability on the left and right sides across the displacement response. Since the depth of the well is small, it allows the harvester to gain an easy jump at a low excitation level from the stable region (see the green ball in Fig. 8) to the unstable region that is shown as a blue ball in the same figure. Under very small excitations, the harvester oscillates inside the well in the stable region (illustrated as green ball in Fig. 8). Once the excitation level is sufficient to pass out the depth well, the harvester will jump from the stable region to the unstable region. The jump causes a chaotic behaviour, as shown is section 5, improving the output power and bandwidth of the harvester in the non-resonance region.

4.2. Mode shape analysis using FEA

This section presents the mode shape analysis to determine the natural frequency of the harvester. This analysis assumes that the harvester is in the planar configuration. Figs. 9 (a) and (b) depict the first two simulated mode shapes of the harvester where the displacement or deformation of the structure occurs along the z axis. Figs. 9 (a) and (b) show that: the red colour means positive

large displacement in z axis, while the blue colour means very small displacement. As illustrated in Fig. 9 (a), the first mode shape (at 9.7 Hz) of the harvester exhibits in-phase movement where all four tip arms and the ortho-planar spring move up with large displacements. In contrast, the second mode shape (at 12.7 Hz) shows that all four tip arms deform with in-phase movement with large deflections, while the proof mass has a very small deflection with counter phase movement relative to all four tip arms, as shown in Fig. 9 (b).

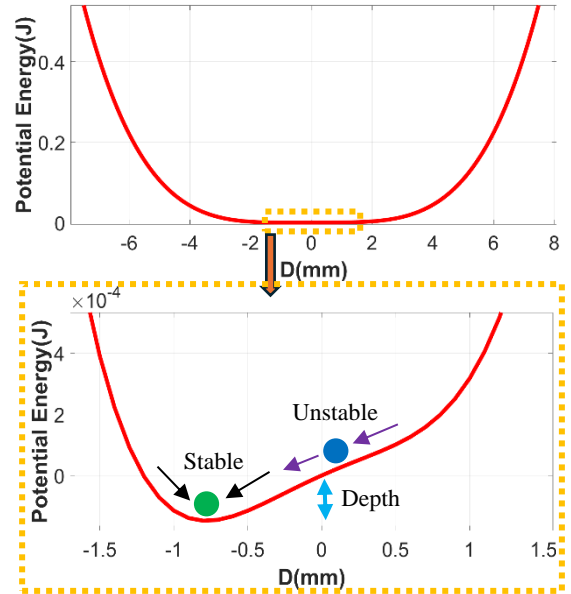


Fig. 8. Potential energy as a function of displacement.

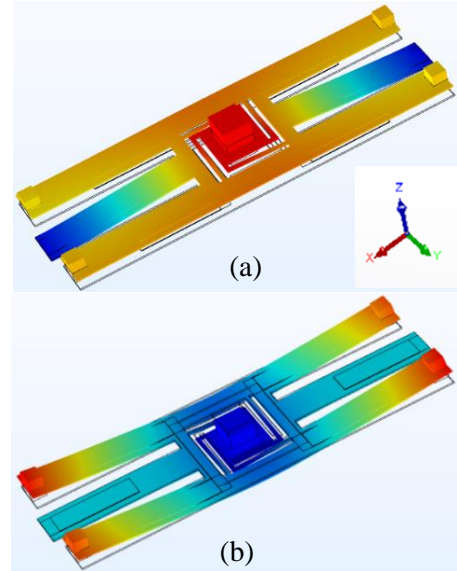


Fig. 9. Simulated mode shapes of the harvester with displacement in the z axis: (a) first mode shape, frequency 9.7 Hz; and (b) second mode shape, frequency 12.7 Hz.

4.3. Dynamical and electrical behaviour of the harvester

To compare the natural frequency of the harvester from the FEA results with linear six DOFs modelling (using equations 1-5) and experimentation, a harmonic excitation signal (0.2 g, 0.4 g, and 0.6 g amplitude) was applied to the harvester. The z-

displacement responses on both the ortho-planar spring (D2) and tip arm (D3) were acquired using the setup shown in subsections 3.2 and 3.3 for modelling and experimentation respectively. The experimental displacement of the harvester relative to the shaker was calculated in the frequency range between 6 Hz and 15 Hz from the measured data. For the six DOFs modelling, the absolute displacement on spring and tip arm was subtracted by the displacement of m_1 to yield the relative displacement. The displacement peak observed in the frequency range is considered as the natural frequency of the harvester. Figs. 10 (a) - (c) show the trend of the displacement response of the harvester on the spring using the three methods.

Fig. 10 (a) and (b) show that the linear FEA model exhibits two natural frequencies at about 9.7 Hz and 13 Hz, and the six

DOFs model also exhibits first and second natural frequencies at 10 Hz and 14.5 Hz, respectively. In Fig. 10 (a), the displacement response of the spring in the FEA simulations shows a discrepancy as the second peak resonance is not visible due to a very small displacement at 13 Hz, while the peak of the second resonance can be seen on the tip arm in the FEA data as shown in Fig. 11 (a). Furthermore, Fig. 10 (c) reveals two main peaks in the experimental data at 9 Hz and 14 Hz under 0.2 g excitation. However, under 0.4 g and 0.6 g acceleration, the first displacement peak shifts to the left from 9 Hz to 8.5 Hz, and the second peak also shifts to the left side from 13.5 Hz to 13 Hz due to the softening nonlinearity.

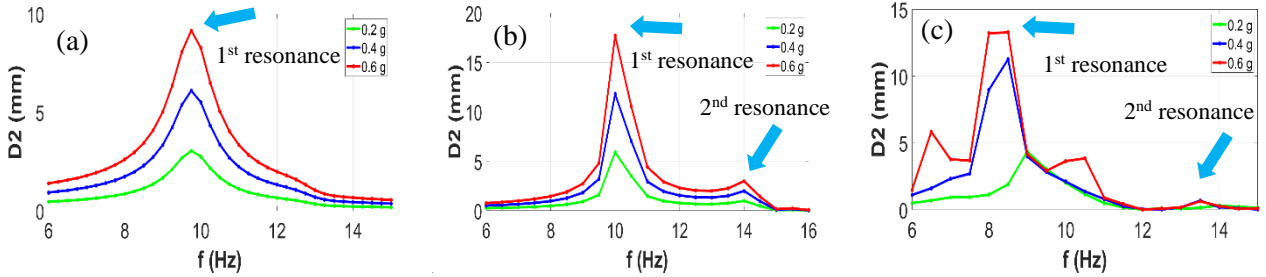


Fig. 10. The amplitude displacement of the spring (D2) as a function of frequency under 0.2 g, 0.4 g, 0.6 g amplitude harmonic excitation in z axis: (a) linear FEA model, (b) linear six DOFs model, and (c) experimentation.

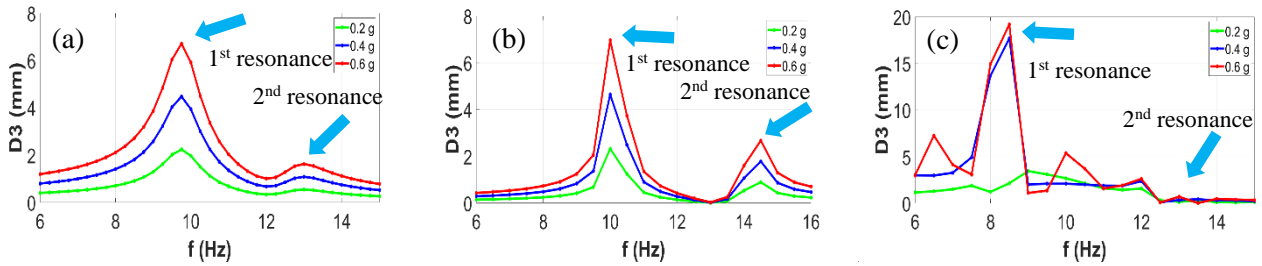


Fig. 11. The amplitude displacement of the tip arm (D3) as a function of frequency under 0.2 g, 0.4 g, 0.6 g amplitude harmonic excitation in z axis: (a) linear FEA model, (b) linear six DOFs model, and (c) experimentation.

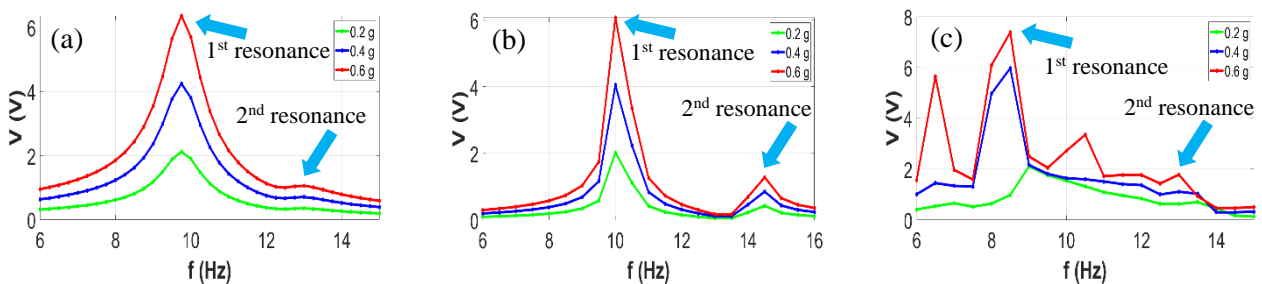


Fig. 12. The amplitude output voltage as a function of frequency of the harvester under 0.2 g, 0.4 g, 0.6 g amplitude harmonic excitation in z axis: (a) linear FEA model, (b) linear six DOFs model, and (c) experimentation.

Two additional peaks also appear, under 0.6 g excitation, at 6.5 Hz due to the multimodal behaviour of the harvester in other directions (x and y axes displacement) [36], and at 10.5 Hz due to chaotic behaviour [24] that will be explained further in subsection 4.4. The linear FEA and linear six DOFs models are capable of predicting the main peaks or natural frequencies of the harvester with a maximum discrepancy below 12%. The two models can also explain the fact that the displacement peak of the first resonance is larger than the peak of the second resonance. The linear analysis is important because it is simple and fast to be applied in the simulation before and during fabrication of the harvester, although it does not capture the nonlinear behaviour evident in the experimentation.

Figs. 11 (a) - (c) show the trend of the tip arm (D3) displacement response of the harvester using the three methods. The tip arm displacement also shows the same trend in the three methods where the first displacement peak is higher than the second one. The displacement of the tip arm in the experimentation also exhibits a similar trend to the displacement of the spring.

The amplitude output voltage of the harvester under harmonic excitation was measured simultaneously with the amplitude displacement, so that the dynamical and electrical behaviour of the harvester could be observed concurrently. Fig. 12 presents the amplitude voltage across frequencies from 6 to 15 Hz from the linear FEA model, linear six DOFS model, and experimentation.

The output voltages of the linear FEA and linear six DOFs models are similar, with a maximum output voltage of about 6 V at the first resonance frequency (about 10 Hz). The second peak voltage is approximately 1 V under 0.6 g excitation, as shown in Fig. 12 (a) and (b) respectively. The large first peak of the first natural frequency appears due to the contribution of both the tip arm and spring displacement peaks in Fig. 10 and 11 respectively. At the second natural frequency, the harvester produces a small second peak voltage due to the small second arm and spring displacement peaks, as shown in Fig. 10 and 11 respectively.

Interestingly, the output voltages from the experimentation exhibit the same trend as both the tip arm and spring displacement. The maximum output voltages from experimentation at the first and second resonant frequencies are almost 8 V and 2 V respectively under 0.6 g excitation. These output voltages are higher than the linear FEA and linear six DOFs approach due to the softening nonlinearity. A peak also occurs at 6.5 Hz with an output voltage that is almost 6 V due to the multimodal behaviour of the harvester. Furthermore, at 10.5 Hz, the peak output voltage is 3.35 V in a non-resonance region. This is due to the chaotic behaviour at the unstable region (Fig. 8). The four peaks (multi-modal), softening nonlinearity, and the chaos increase the performance and bandwidth of the harvester under the harmonic excitation.

4.4. Chaotic analysis on nonlinear six DOFs and experimentation under harmonic excitation

The previous subsection shows that the experimentation exhibits an interesting peak at 10.5 Hz in a non-resonance region where the harvester exhibits chaotic behaviour. In this subsection, displacement-velocity phase portraits are employed to understand the phenomenon, with the velocity being derived from the displacement.

Data from the nonlinear six DOFs model (using equations 1-5) is also introduced to analyse the chaotic behaviour at 9.6 Hz. Fig. 13 shows the tip arm displacement (D3)-time plot and displacement-velocity phase portrait of the harvester from the nonlinear analytical model and experimentation. As shown in Fig. 13 (a), the displacement-time responses under 0.2 g and 0.4 g excitation are perfect harmonics, but the displacement response under 0.6 g excitation shows chaotic behaviour from 0.8 s to 1.5 s. Fig. 13 (c) shows that the chaotic manner occurs using a nonlinear analytical model. Under 0.2 g and 0.4 g harmonic excitation at 9.6 Hz, the harvester stays in the stable region as the displacement-velocity phase portrait features a single lobe. However, under 0.6 g excitation, the harvester exhibits chaotic behaviour as the displacement-velocity phase portrait shows two distinctive lobes where the harvester jumps from the stable region to the unstable region. This chaotic behaviour is caused by the interaction of the six degrees of freedom of motion and the softening nonlinearity in the system.

The predictions of the nonlinear six DOFs model was then validated through experimentation. Fig. 13 (b) shows that under 0.2 g and 0.4 g excitation, the tip arm displacement responses are also a perfect harmonic, but under 0.6 g, the displacement response becomes chaotic. For example, from 0.7 s to 0.85 s, the displacement response is not a perfect harmonic, and the harvester oscillates in the stable state; while from 0.85 s to 1 s, the displacement response shows a large magnitude due to the jump from the stable state to the unstable state, resulting a large output voltage at 10.5 Hz in Fig. 12 (c). Unlike in the analytical modelling, the jump in the experimentation is caused by a physical jump from one stable position to the unstable position (see Fig. 14). Then, the displacement-velocity phase portrait is plotted in Fig 13 (d). At the tip arm, the harvester also exhibits

mono-stability under 0.2 g and 0.4 g excitation where the displacement-velocity phase portrait shows a single lobe as shown in Fig. 13 (d). However, under 0.6 g excitation, a chaotic manner is evident in which the harvester jumps from the stable region to the unstable region in Fig. 13 (d). The two distinctive lobes arise due to the asymmetry of the potential energy function in Fig. 8.

Fig. 14 illustrates the stable state (under 0.2 and 0.4 g) and the unstable state (under 0.6 g) behaviour of the harvester that occurs in the experimentation, captured using a high-speed camera. The stable behaviour shows that the four tip arms and ortho-planar spring oscillate around the buckled-down condition. They do not pass the planar or initial state before the gravitational pre-load, as shown in Fig. 14 (a). The 0.2 g and 0.4 g excitation are insufficient to drive the harvester from stable state to the unstable region.

In contrast, the unstable behaviour, as illustrated in Fig 14 (b), shows that the harvester can pass the planar or initial state (the buckled-up condition), and the four tip arms and the ortho-planar spring oscillate around the planar state under 0.6 g excitation which is sufficient to drive the harvester from the stable region to the unstable region (chaotic behaviour).

5. The analysis of the harvester using nonlinear analytical modelling and experimentation under sine sweep excitation

This section presents the analysis of the harvester under sine sweep excitation using nonlinear six DOFs modelling (using equations 1-5) and experimentation in order to verify the occurrence of nonlinear and chaotic behaviour. In the first subsection, the dynamical characteristic (displacement) of the harvester is investigated under sine sweep excitation, and the electrical characteristics (power) and bandwidth analysis under sine sweep excitation are examined in the second subsection. In the last subsection, normalised power density (NPD) is evaluated to compare with the previous low-frequency PVEHs in the literature.

5.1. Dynamical characteristic of the harvester under sine sweep excitations

The dynamical behaviour of the harvester was characterised analytically and experimentally to determine the nonlinear and chaotic behaviour of the harvester under sine sweep excitation. The frequency range for forward (Fwd) and backward (Bwd) sweeps was between 6 Hz and 15 Hz. A slow sweep rate of 4.8 Hz/min was chosen to excite the nonlinear behaviour of the harvester [14,53]. The amplitude displacement of the tip arm was considered to determine the dynamical behaviour of the harvester under acceleration amplitudes of 0.2 g, 0.4 g, and 0.6 g. Those amplitudes were chosen in order to investigate the nonlinear and chaotic behaviour of the harvester under a low level of excitation where most of broadband ambient vibrations occur.

Figs. 15 (a) – (f) illustrate the amplitude displacement of the harvester measured on the tip arm for the nonlinear six DOFs model and experimentation. Table 3 summarises the peak of the displacement measured on the tip arm under frequency sweeps. Figs. 15 (a), (c), and (e) show that the peak of the displacement of the tip arm of the harvester for the nonlinear six DOFs model shifts from 9.8 Hz (0.2 g) to 9.1 Hz (0.4 g), and 8.5 Hz (0.6 g) respectively for backward sweeps; while for forward sweeps, the peak of the displacement of the tip arm shifts from 10.1 Hz (0.2 g) to 9.8 Hz (0.4 g), and 9.5 Hz (0.6 g) respectively, as can be observed in Figs. 15 (a), (c), and (e).

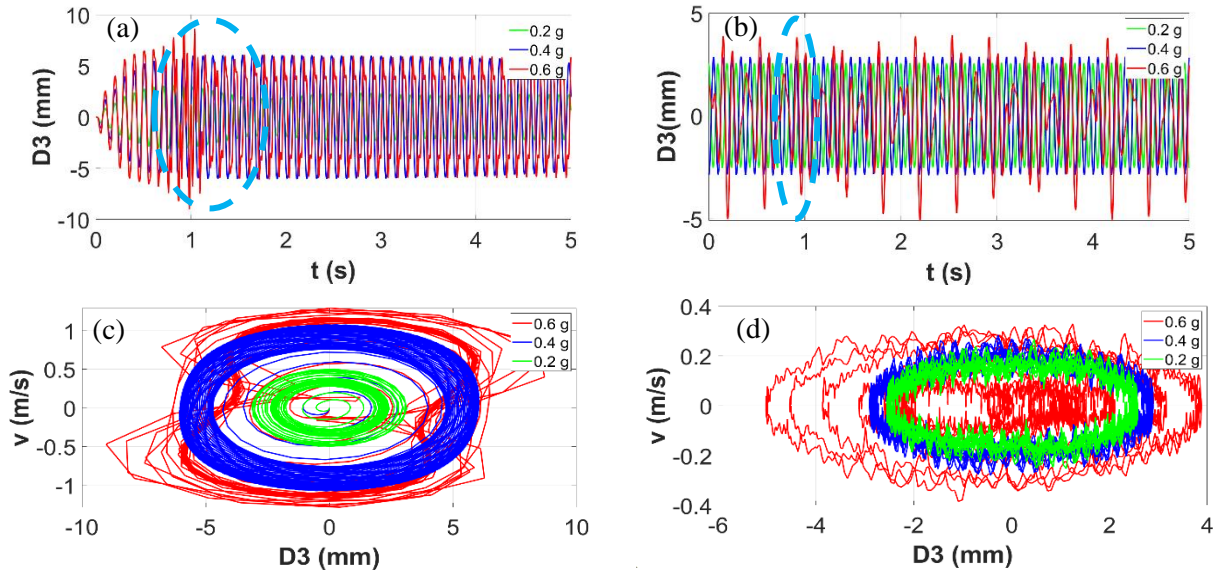


Fig. 13. Displacement-time and displacement-velocity phase portraits of the harvester under 0.2, 0.4, and 0.6 g amplitude harmonic excitation on the tip arm (D3) in z axis: (a) displacement as a function of time, (c) displacement-velocity portrait of the nonlinear six DOFs at 9.6 Hz; (b) displacement as a function of time, (d) displacement-velocity portrait of the experimentation at 10.5 Hz.

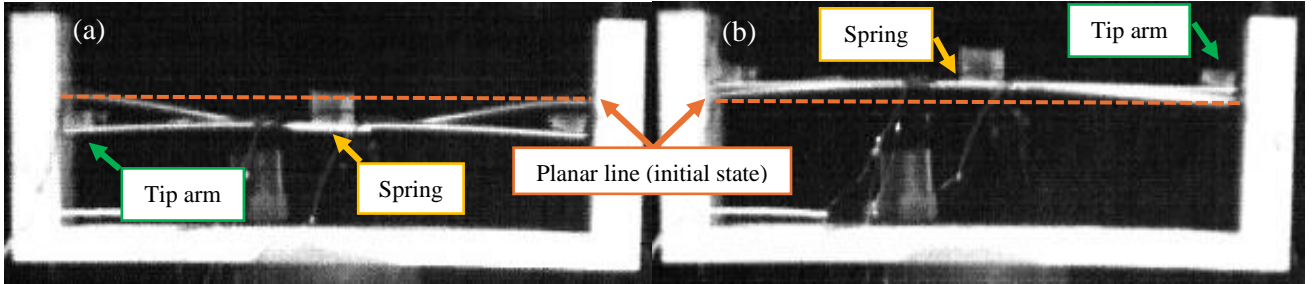


Fig. 14. The side view of the stable and unstable behaviour of the harvester: (a) stable behaviour under 0.2 g and 0.4 g; (b) unstable behaviour under 0.6 g.

Table 3. The peak of the displacement measured on the tip arm of the harvester under frequency sweeps for the nonlinear six DOFs model and experimentation.

	The peak of the displacement of the harvester					
	Backward			Forward		
	0.2 g	0.4 g	0.6 g	0.2 g	0.4 g	0.6 g
Nonlinear six DOFs (Hz)	9.8	9.1	8.5	10.1	9.8	9.5
Experimentation (Hz)	7.9	7.1	6.8	9	7.1	6.8

Moreover, the experimental peak of the displacement of the tip arm, under 0.2 g excitation in Fig. 15 (b) shifts from 7.9 Hz to 7.1 Hz (0.4 g), and 6.8 Hz (0.6 g) respectively (Fig. 15 (d) and (f)) for backward sweeps. Under forward sweeps, the peak of the displacement also shifts to the left from 9 Hz (0.2 g) to 7.1 Hz (0.4 g), and 6.8 Hz (0.6 g) respectively. The shifting to the left of the experimental peak of the displacement with increasing acceleration is due to the softening nonlinearity that is more dominant than the hardening nonlinearity as shown in Fig. 7.

The simplified nonlinear six DOFs model that only considers the softening nonlinear part can be used to predict the trend of the peak of the displacement when the excitation increases.

Interestingly, under 0.6 g sine sweep excitation, the displacement responses of both the six DOFs model, and experimentation start showing chaotic behaviour. In Fig. 15 (e), the simulated displacement response of the tip arm under 0.6 g shows chaotic behaviour at 9.6 Hz. Furthermore, the experimental data also exhibit chaotic behaviour from 8.7 Hz to 11.4 Hz under 0.6 g forward and backward sweeps. The chaotic behaviour could increase the displacement in the non-resonance region, leading to improvements in both the output power and bandwidth of the harvester.

5.2. Electrical characteristics (power) and bandwidth analysis of the harvester under sine sweep excitations

In this section, electrical characteristics (power) and bandwidth analysis of the harvester using nonlinear six DOFs modelling and experimentation are described to analyse the peak of the output power and bandwidth of the harvester under sine sweep excitations. The amplitude output power of the harvester was recorded simultaneously with the amplitude displacement response in order to fully understand the mechanical and electrical behaviour of the harvester under frequency sweeps.

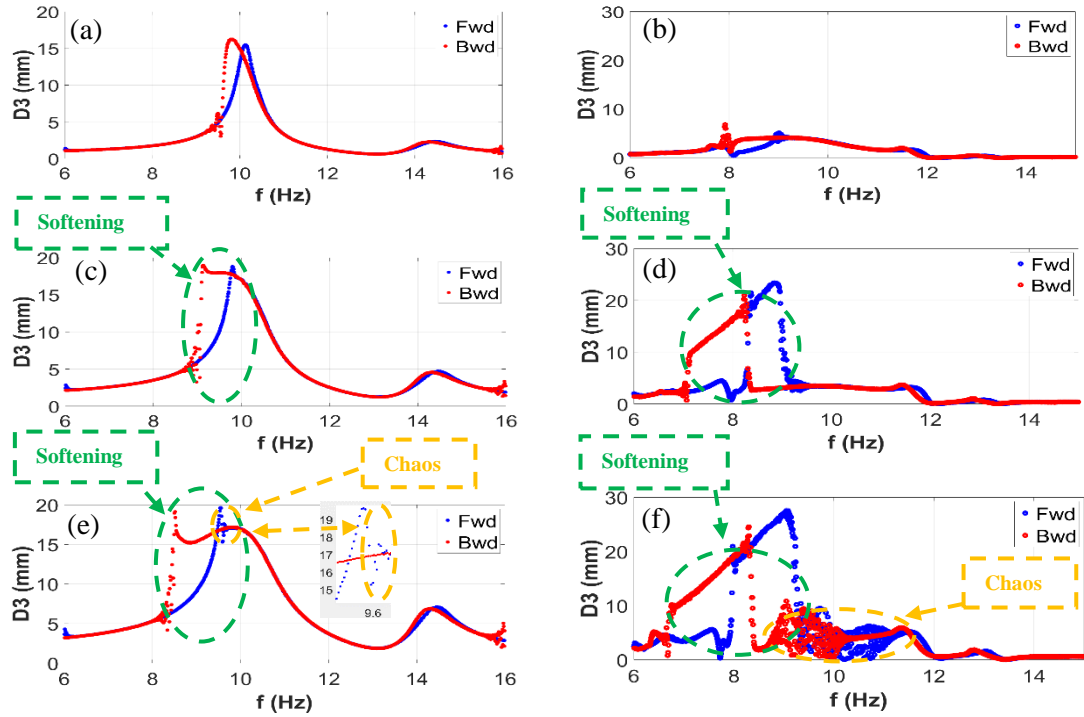


Fig. 15. The amplitude displacement of the harvester in the z axis on the tip arm under frequency sweeps for nonlinear six DOFs at (a) 0.2 g, (c) 0.4 g, (e) 0.6 g, and for experimentation at (b) 0.2 g, (d) 0.4 g, (f) 0.6 g.

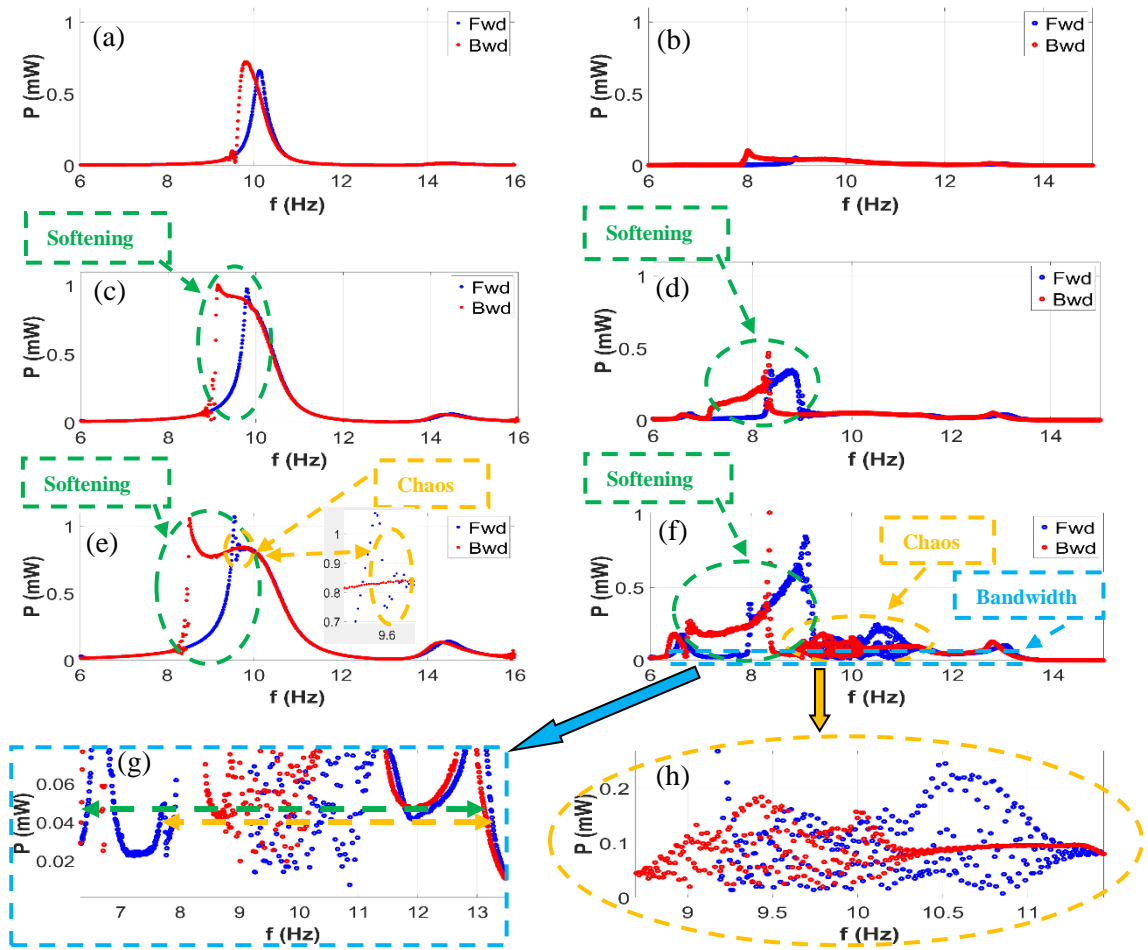


Fig. 16. The amplitude output power of the harvester under frequency sweeps for nonlinear six DOFs model at (a) 0.2 g, (c) 0.4 g, (e) 0.6 g, and for experimentation at (b) 0.2 g, (d) 0.4 g, (f) 0.6 g, (g) 0.6 g bandwidth, (h) 0.6 g chaos.

Figs. 16 (a) – (f) present the amplitude output power of the harvester under frequency sweeps of amplitude 0.2 g, 0.4 g, and 0.6 g between 6 Hz and 15 Hz. Table 4 summarises the peak of the output power of the harvester under frequency sweeps. Figs. 16 (a), (c) and (e) show that the peak of output power of the harvester in the nonlinear six DOFs model under 0.2 g at 9.8 Hz shifts toward the left to 9.1 Hz under 0.4 g and to 8.5 Hz under 0.6 g for backward sweeps respectively. Under the forward sweeps, the peak of output power also shifts toward the left from 10.1 Hz (0.2 g) to 9.8 Hz (0.4 g), and to 9.6 Hz (0.6 g) respectively.

Table 4. The peak of the output power of the harvester under frequency sweeps for nonlinear six DOFs and experimentation.

	The peak of the output power of the harvester					
	Backward			Forward		
	0.2 g	0.4 g	0.6 g	0.2 g	0.4 g	0.6 g
Nonlinear six DOFs (Hz)	9.8	9.1	8.5	10.1	9.8	9.6
Experimentation (Hz)	8	7.2	6.8	9	8.3	8

Similarly, as shown in Figs. 16 (b), (d), and (f) for the experimental data, the peak of the output power also shifts from 8 Hz at 0.2 g to 7.2 Hz at 0.4 g, and to 6.8 Hz at 0.6 g respectively for backward sweeps. The peak of the output power also shifts from 9 Hz (0.2 g) to 8.3 Hz (0.4 g), and to 8 Hz (0.6 g) respectively under forward sweeps. The harvester also shows a peak at 6.6 Hz and 6.4 Hz under 0.4 g and 0.6 g respectively, which is similar to what was observed under harmonic excitation in Fig. 12 (c), due to the multi-modal behaviour of the harvester. Both the nonlinear six DOFs model and the experimentation exhibit softening nonlinearity in the output power which is consistent with the dynamical behaviour shown in Fig. 15.

Moreover, under 0.6 g sine sweep excitation, both the simulated and experimental peak of the output power also starts to show chaotic behaviour. In Fig. 16 (e), the simulated amplitude of the output power under 0.6 g shows chaotic behaviour at 9.6 Hz. The experimental data also exhibits similar behaviour from 8.7 Hz to 11.4 Hz under 0.6 g forward and backward sweeps. The chaotic behaviour increases the displacement in the non-resonance region, leading to improvements in both the amplitude of the output power (0.24 mW) and bandwidth (1.84 Hz) of the harvester in this region under the 0.6 g forward sweep as shown in Fig. 16 (h).

Interestingly, Figs. 16 (g) and (h) show that, under 0.6 g forward sweep, the softening nonlinearity and the chaotic behaviour improve the bandwidth of the harvester up to a 5.6 Hz bandwidth, from 7.6 Hz to 13.2 Hz, with an average power more than 41 μ W (see the orange dashed double arrow). Under the 0.6 g backward sweep, the harvester achieved a maximum bandwidth of 6.8 Hz, from 6.3 Hz to 13.1 Hz, with an average power that is higher than 46 μ W (see the green dashed double arrow) as seen in Fig. 16 (g). Harvested power levels of 41 μ W and 46 μ W are sufficient for powering commercial IoT sensors where the average demand is 18 μ W [54].

The maximum 6.8 Hz bandwidth under 0.6 g backward sweep was achieved by the harvester due to the chaotic behaviour that occurs between the first (P1) and the second (P3) resonant frequency, and due to the first peak at 6.4 Hz (multi-modal behaviour in other directions [36]), as illustrated in Fig. 17. The softening nonlinearity also enhances the bandwidth of the harvester as the power response shifts to the left side of the frequency range when the excitation increases.

The six DOFs model is able to predict the softening nonlinearity and the chaotic behaviour that occurs in the experimentation. However, the discrepancy occurs in the duration

and location of the chaos across the frequency. For example, in the six DOFs modelling, chaos only appears at around 9.6 Hz near the first resonant frequency, while in the experiment, chaos occurs from 8.7 Hz to 11.4 Hz which lies between the first (P1) and second (P3) resonant frequencies (Fig. 17). This discrepancy is due to the simplification of the six DOFs model. Nevertheless, the analytical model can be still utilised to optimise the harvester using parametric studies.

Furthermore, Fig. 17 (a) and (b) show the amplitude output power corresponding to the -3dB bandwidth (half power bandwidth) for the nonlinear six DOFs model and the experimentation respectively. Table 5 summarises the peak of the output power and bandwidth of the harvester under 0.6 g frequency sweeps as seen in Figs. 17 (a) and (b). Fig. 17 (a) shows that the maximum peak of the output power of the harvester in the six DOFs model reached 1.07 mW (P1 (F)) at 9.5 Hz and 1.06 mW (P1 (B)) at 8.5 Hz under forward and backward sweeps, respectively. At the second the peak (P2), the harvester generates a peak of the output power of 0.84 mW with a maximum bandwidth of 2.2 Hz under backward sweeps.

Similarly, in the experimentation, the harvester gains a maximum peak of the output power of 0.84 mW (P1 (F)) and 1.01 mW (P1 (B)) under forward and backward sweeps, respectively, as shown in Fig. 17 (b). On the second peak, P2, the harvester generates a peak power of 0.38 mW with 1.3 Hz bandwidth under forward sweeps, while it generates a peak power of 0.26 mW with a maximum 2.02 Hz bandwidth under backward sweeps. The maximum power and bandwidth for nonlinear six DOFs modelling and experimentation were achieved due to the softening nonlinearity that shifts the peak of the output power to the left side (lower frequency). Moreover, the analytical modelling and experimentation shows a similar frequency shift and peak power at the first and second resonant frequencies. All of the peak power levels are sufficient for powering commercial IoT sensors, making the harvester suitable to harvest broadband ambient vibrations in low frequency regions.

5.3. Comparison of the proposed harvester with the previous low-frequency PVEHs in the literature using NPD

This section presents a comparison of the proposed harvester with the previous low-frequency PVEHs in the literature using the normalised power density (NPD) in the low frequency range (below 55 Hz). NPD is commonly used to compare piezoelectric vibrational energy harvesters (PVEHs) in the literature [55,56] and it is defined as:

$$NPD = \frac{Power}{Volume \times acceleration^2} \quad (10)$$

Where power is the amplitude output power (μ W), volume is the volume of the harvester (cm^3), and acceleration is the excitation (g).

This paper only considers the PVEHs using PZT piezoelectric materials in the frequency range below 55 Hz. The effective total volume in this study encompasses all proof masses, structures, and PZT volume including the substrate of the bimorph beam. It is noteworthy that no standard has yet been established to determine the total volume of PVEHs [20,57]. There are three categories of the total volume of the PVEHs that are effective volume [57], vibration volume [58], and package volume [24] in the literature. However, the NPD (that considers the different categories of the total volume) remains important to accommodate the different PVEHs designs, sizes, and working principles in the literature, and to compare the latest development of the proposed harvester in the future. Table 6 reports the proposed harvester compared with previous published PVEHs in the literature using NPD.

Table 5. Result summaries of the peak power and bandwidth of the proposed harvester using nonlinear six DOFs and experimentation.

	Sweeps	a (g)	f1 (Hz)	P1 (mW)	f2 (Hz)	P2 (mW)	-3 dB bandwidth P2 (Hz)	f3 (Hz)	P3 (mW)	-3 dB bandwidth P3 (Hz)
Nonlinear six DOFs	Fwd	0.6	9.5	1.07	9.9	0.82	1.36	14.4	0.14	0.95
	Bwd		8.5	1.06	9.8	0.84	2.2	14.3	0.14	1.1
Experimentation	Fwd	0.6	9	0.84	7.9	0.38	1.3	13	0.1	0.92
	Bwd		8.3	1.01	6.7	0.26	2.02	12.7	0.12	0.64

Table 6. Comparison of the proposed harvester with the previous low-frequency PVEHs in the literature.

	f (Hz)	a (g)	Peak power (μW)	Volume (cm^3)	Power density ($\mu\text{W cm}^{-3}$)	NPD ($\mu\text{W cm}^{-3} \text{g}^{-2}$)
This work (Bwd)*	8.3	0.6	1010	14.67	68.8	191.2
This work (Fwd)*	9	0.6	840	14.67	57.3	159.1
[59]**	2	2	43	1.85	23.2	5.8
[60]***	2.03	0.26	13290	1156	11.5	170.1
[61]*	4	1	40	12	3.3	3.3
[24]***	6.2	1.2	2200	660	3.3	2.3
[25]***	4	0.7	143	144	0.9	2
[58]**	12	0.1	442	8.4	52.6	5261.9
[35]*	16	0.4	740	3.0369 *estimated	243.6	1522.9
[62]*	20.1	0.4	1530	16.416	93.2	582.5
[63]*	23.5	0.5	63	3.42	18.4	73.6
[64]*	26	0.08	280	50	5.6	875
[65]*	26.375	0.17	122	21.28	5.7	198.3
[66]*	27	0.05	29.3	3.106	9.4	3773.3
[57]*	29	0.69	15300	1.14	13421.1	28189.5
[67]*	45.6	1	23900	3.52	6789.7	6789.7
[68]*	47	1	0.0855	0.0101	8.4	8.4
[69]*	49.7	0.2	118	0.588	200.6	5017
[70]**	49.8	0.1	6.7	0.0573	116.9	11692.8

*Effective volume (EV), **Vibration volume (VV), ***Package volume (PV)

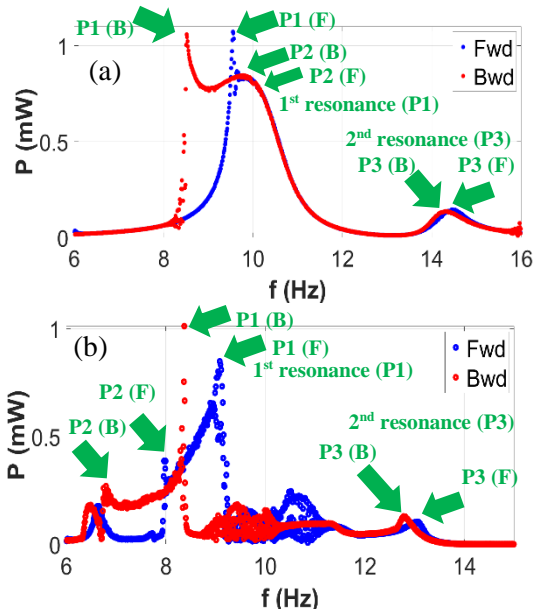


Fig. 17. The output power of the harvester as a function of frequency under 0.6 g (amplitude) in (a) nonlinear six DOFs model, and (b) experimentation.

Fig. 18 illustrates NPD as a function of frequency below 55 Hz, as reported in Table 6. It is evident that the proposed harvester (see the red stars) compares favourably with typical low-

frequency PVEHs (blue stars) using the same PZT piezoelectric materials and effective volume. The proposed harvester achieves a maximum 191.2 NPD ($\mu\text{W cm}^{-3} \text{g}^{-2}$) under 0.6 g backward sweeps at 8.3 Hz with a maximum 68.8 power density ($\mu\text{W cm}^{-3}$). Under 0.6 g forward sweeps at 9 Hz, the proposed harvester produces a maximum 159.1 NPD ($\mu\text{W cm}^{-3} \text{g}^{-2}$) with 57.3 power density ($\mu\text{W cm}^{-3}$). The proposed harvester exhibits an NPD that compares favourably in low frequency region (<10 Hz) in the literature.

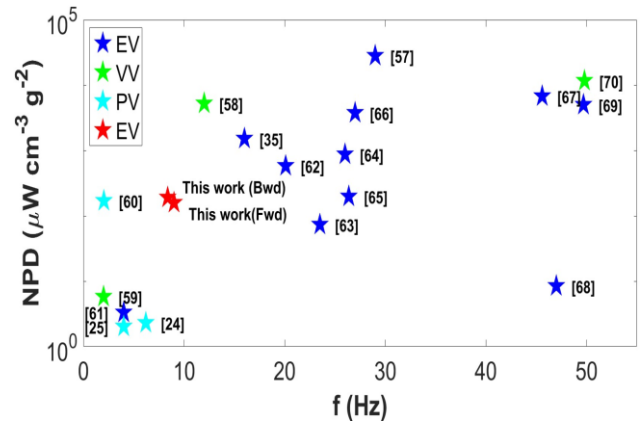


Fig. 18. Comparison of the normalised power density (NPD) of the proposed harvester with recently published low-frequency PVEHs.

6. Conclusion

A novel nonlinear and asymmetric monostable COPS-PVEH using a H-I structure is presented for harvesting low-frequency range ambient vibrations (below 15 Hz) in the gravity (vertical) direction. The harvester has been designed and analysed using FEA, six DOFs analytical modelling, and experimentation. The natural frequency from FEA, analytical modelling, and experimentation shows good agreement in the first and second natural frequencies of the harvester with a maximum discrepancy below 12%. It is also observed that the linear FEA and linear six DOFs model show a maximum peak output voltage of about 6 V at around 10 Hz under 0.6 g harmonic excitation. The maximum of the peak output voltage from experimentation is almost 8 V, which is higher than the linear FEA and linear six DOFs models, under 0.6 g harmonic excitation at 8.5 Hz due to a softening nonlinearity. Nevertheless, the linear FEA and linear six DOFs models could still be utilised to optimise the harvester using parametric studies, and to achieve the desired resonance frequency with specific mode shapes. Two additional peaks also appear at 6.5 Hz (due to multi directional behaviour) and at 10.5 Hz (due to chaotic behaviour) under 0.6 g harmonic excitation, which help to widen the bandwidth of the harvester.

Furthermore, the harvester exhibits softening nonlinearity caused by a buckled-down 5 mm configuration (pre-load due to gravitation) and the ortho-planar structure due to the dominant axial (inertial) force, as observed using frequency sweeps at acceleration amplitudes of 0.2 g, 0.4 g, and 0.6 g. The harvester also reveals chaotic behaviour, due to an asymmetric elastic potential function at the unstable region, improving the peak of output power (up to 0.24 mW) and bandwidth (up to 1.84 Hz) of the harvester. The maximum peak of the output power recorded was 1.07 mW and 1.01 mW at the first resonant frequency for the nonlinear six DOFs modelling and experimentation respectively under 0.6 g sine sweep excitation. Experimentally, the harvester achieves a maximum bandwidth of 6.8 Hz (from 6.3 Hz to 13.1 Hz) with an average peak power that is higher than 46 μ W. The proposed harvester also compares favourably, using NPD metrics, to typical PVEHs in the low frequency range (<10 Hz) in the literature. Finally, the multi-modal, softening nonlinearity and chaotic behaviour have been shown to enhance the performance and bandwidth of the harvester in the low excitation level (amplitude of 0.2 g, 0.4 g, and 0.6 g acceleration) and low frequency (sub 15 Hz) range where broadband ambient vibrations are abundant in many applications.

Credit authorship contribution statement

Ibnu Taufan: Conceptualization, Methodology, Data curation, Validation, Writing – original draft. **Jeff Punch:** Supervision, Writing - review & editing. **Valeria Nico:** Conceptualization, Writing - review & editing, Supervision, Funding acquisition, Project administration.

Declaration of Competing Interest

The authors declare that they have no conflict of interest.

Data availability

Data will be made available through UL repository.

Acknowledgments

The authors acknowledge the financial support of Science Foundation Ireland under Grant No. 21/PATH-S/9510 and 13/RC/2077_P2.

Appendix A. Supplementary material

Supplementary data to this article can be found online at <https://doi.org/10.1016/j.sna.2024.115984>.

References

- [1] Gubbi J, Buyya R, Marusic S, Palaniswami M. Internet of Things (IoT): A vision, architectural elements, and future directions. *Future Generation Computer Systems* 2013;29:1645–60. <https://doi.org/10.1016/j.future.2013.01.010>.
- [2] Deng L, Fang Y, Wang D, Wen Z. A MEMS based piezoelectric vibration energy harvester for fault monitoring system. *Microsystem Technologies* 2018;24:3637–44. <https://doi.org/10.1007/s00542-018-3784-7>.
- [3] Damodaram D, Godi RK, Rajkumar, Divakara Rao D V., Glory KB, Somu K. Power control management system model using wireless sensor network. *Measurement: Sensors* 2023;25. <https://doi.org/10.1016/j.measen.2022.100639>.
- [4] Nico V, O'Donoghue D, Frizzell R, Kelly G, Punch J. A Multiple Degree-of-Freedom Velocity-Amplified Vibrational Energy Harvester Part B: Modelling. *Smart Materials, Adaptive Structures and Intelligent Systems* 2014. <https://doi.org/https://doi.org/10.1115/SMASIS2014-7511>.
- [5] Roundy S, Steingart D, Frechette L, Wright P, Rabaey J. Power Sources for Wireless Sensor Networks. *European Workshop on Wireless Sensor Networks 2004*. https://doi.org/10.1007/978-3-540-24606-0_1.
- [6] Dewan A, Ay SU, Karim MN, Beyenal H. Alternative power sources for remote sensors: A review. *J Power Sources* 2014;245:129–43. <https://doi.org/10.1016/j.jpowsour.2013.06.081>.
- [7] Erturk A, Inman DJ. On mechanical modeling of cantilevered piezoelectric vibration energy harvesters. *J Intell Mater Syst Struct* 2008;19:1311–25. <https://doi.org/10.1177/1045389X07085639>.
- [8] Sun S, Tse PW. Modeling of a horizontal asymmetric U-shaped vibration-based piezoelectric energy harvester (U-VPEH). *Mech Syst Signal Process* 2019;114:467–85. <https://doi.org/10.1016/j.ymsp.2018.05.029>.
- [9] Twiefel J, Westermann H. Survey on broadband techniques for vibration energy harvesting. *J Intell Mater Syst Struct*, vol. 24, 2013, p. 1291–302. <https://doi.org/10.1177/1045389X13476149>.
- [10] Amri M, Basset P, Cottone F, Galayko D, Najjar F, Bourouina T. Novel nonlinear spring design for wideband vibration energy harvesters. *PowerMEMS* 2011.
- [11] Dhote S, Zu J, Zhu Y. A nonlinear multi-mode wideband piezoelectric vibration-based energy harvester using compliant orthoplanar spring. *Appl Phys Lett* 2015;106. <https://doi.org/10.1063/1.4919000>.
- [12] Dhote S, Li H, Yang Z. Multi-frequency responses of compliant orthoplanar spring designs for widening the bandwidth of piezoelectric energy harvesters. *Int J Mech Sci* 2019;157–158:684–91. <https://doi.org/10.1016/j.ijmecsci.2019.04.029>.
- [13] Mann BP, Owens BA. Investigations of a nonlinear energy harvester with a bistable potential well. *J Sound Vib* 2010;329:1215–26. <https://doi.org/10.1016/j.jsv.2009.11.034>.
- [14] Stanton SC, McGehee CC, Mann BP. Nonlinear dynamics for broadband energy harvesting: Investigation of a bistable piezoelectric inertial generator. *Physica D* 2010;239:640–53. <https://doi.org/10.1016/j.physd.2010.01.019>.

- [15] Su WJ, Zu J, Zhu Y. Design and development of a broadband magnet-induced dual-cantilever piezoelectric energy harvester. *J Intell Mater Syst Struct* 2014;25:430–42. <https://doi.org/10.1177/1045389X13498315>.
- [16] Harnie RL, Wang KW. A review of the recent research on vibration energy harvesting via bistable systems. *Smart Mater Struct* 2013;22. <https://doi.org/10.1088/0964-1726/22/2/023001>.
- [17] Daqaq MF, Masana R, Erturk A, Quinn DD. On the role of nonlinearities in vibratory energy harvesting: A critical review and discussion. *Appl Mech Rev* 2014;66. <https://doi.org/10.1115/1.4026278>.
- [18] Fan K, Chang J, Pedrycz W, Liu Z, Zhu Y. A nonlinear piezoelectric energy harvester for various mechanical motions. *Appl Phys Lett* 2015;106. <https://doi.org/10.1063/1.4922212>.
- [19] Tran N, Ghayesh MH, Arjomandi M. Ambient vibration energy harvesters: A review on nonlinear techniques for performance enhancement. *Int J Eng Sci* 2018;127:162–85. <https://doi.org/10.1016/j.ijengsci.2018.02.003>.
- [20] Liang H, Hao G, Olszewski OZ. A review on vibration-based piezoelectric energy harvesting from the aspect of compliant mechanisms. *Sens Actuators A Phys* 2021;331. <https://doi.org/10.1016/j.sna.2021.112743>.
- [21] Nan W, Yuncheng H, Jiyang F. Bistable energy harvester using easy snap-through performance to increase output power. *Energy* 2021;226. <https://doi.org/10.1016/j.energy.2021.120414>.
- [22] Chen K, Ding X, Tian L, Shen H, Song R, Bian Y, et al. An M-shaped buckled beam for enhancing nonlinear energy harvesting. *Mech Syst Signal Process* 2023;188. <https://doi.org/10.1016/j.ymsp.2022.110066>.
- [23] Wu Z, Xu Q. Design of a structure-based bistable piezoelectric energy harvester for scavenging vibration energy in gravity direction. *Mech Syst Signal Process* 2021;162. <https://doi.org/10.1016/j.ymsp.2021.108043>.
- [24] Hou C, Zhang X, Yu H, Shan X, Sui G, Xie T. Ori-inspired bistable piezoelectric energy harvester for scavenging human shaking energy: Design, modeling, and experiments. *Energy Convers Manag* 2022;271. <https://doi.org/10.1016/j.enconman.2022.116309>.
- [25] Zhou J, Zhao X, Wang K, Chang Y, Xu D, Wen G. Bio-inspired bistable piezoelectric vibration energy harvester: Design and experimental investigation. *Energy* 2021;228. <https://doi.org/10.1016/j.energy.2021.120595>.
- [26] Li Q, Bu L, Lu S, Yao B, Huang Q, Wang X. Practical asymmetry and its effects on power and bandwidth performance in bi-stable vibration energy harvesters. *Mech Syst Signal Process* 2024;206. <https://doi.org/10.1016/j.ymsp.2023.110939>.
- [27] Norenberg JP, Luo R, Lopes VG, Peterson JVLL, Cunha A. Nonlinear dynamics of asymmetric bistable energy harvesters. *Int J Mech Sci* 2023;257. <https://doi.org/10.1016/j.ijmecsci.2023.108542>.
- [28] Kumar A, Ali SF, Arockiarajan A. Exploring the benefits of an asymmetric monostable potential function in broadband vibration energy harvesting. *Appl Phys Lett* 2018;112. <https://doi.org/10.1063/1.5037733>.
- [29] Parise JJ, Howell LL, Magleby SP. Ortho-planar linear-motion springs. *Mech Mach Theory* 2001;36:1281–1299. [https://doi.org/10.1016/S0094-114X\(01\)00051-9](https://doi.org/10.1016/S0094-114X(01)00051-9).
- [30] Mallick D, Amann A, Roy S. A nonlinear stretching based electromagnetic energy harvester on FR4 for wideband operation. *Smart Mater Struct* 2015;24. <https://doi.org/10.1088/0964-1726/24/1/015013>.
- [31] Mohammadi A, Sadrafsari S, Shokrani A, Bowen CR. Asymmetric Quad Leg Orthoplanar Spring for Wideband Piezoelectric Micro Energy Harvesting. *Proceedings of the IEEE International Conference on Micro Electro Mechanical Systems (MEMS)*, vol. 2023- January, Institute of Electrical and Electronics Engineers Inc.; 2023, p. 697–700. <https://doi.org/10.1109/MEMS49605.2023.10052512>.
- [32] Gafforelli G, Xu R, Corigliano A, Kim SG. Modeling of a Bridge-Shaped Nonlinear Piezoelectric Energy Harvester. *Energy Harvesting and Systems* 2014;1:179–87. <https://doi.org/10.1515/ehs-2014-0005>.
- [33] Boisseau S, Despesse G, Seddik BA. Nonlinear h-shaped springs to improve efficiency of vibration energy harvesters. *Journal of Applied Mechanics, Transactions ASME* 2013;80. <https://doi.org/10.1115/1.4023961>.
- [34] Wang D, Lu H, Deng L, Zhang D. An H-shaped two-dimensional piezoelectric vibration energy harvester. *Jpn J Appl Phys* 2019;58. <https://doi.org/10.7567/1347-4065/ab4074>.
- [35] Toyabur RM, Salauddin M, Park JY. Design and experiment of piezoelectric multimodal energy harvester for low frequency vibration. *Ceram Int* 2017;43:S675–81. <https://doi.org/10.1016/j.ceramint.2017.05.257>.
- [36] Sun R, Li Q, Yao J, Scarpa F, Rossiter J. Tunable, multi-modal, and multi-directional vibration energy harvester based on three-dimensional architected metastructures. *Appl Energy* 2020;264. <https://doi.org/10.1016/j.apenergy.2020.114615>.
- [37] Huang D, Zhou S, Litak G. Theoretical analysis of multi-stable energy harvesters with high-order stiffness terms. *Commun Nonlinear Sci Numer Simul* 2019;69:270–86. <https://doi.org/10.1016/j.cnsns.2018.09.025>.
- [38] Pellegrini SP, Tolou N, Schenk M, Herder JL. Bistable vibration energy harvesters: A review. *J Intell Mater Syst Struct*, vol. 24, 2013, p. 1303–12. <https://doi.org/10.1177/1045389X12444940>.
- [39] Erturk A, Inman DJ. Broadband piezoelectric power generation on high-energy orbits of the bistable Duffing oscillator with electromechanical coupling. *J Sound Vib*, vol. 330, 2011, p. 2339–53. <https://doi.org/10.1016/j.jsv.2010.11.018>.
- [40] Litak G, Friswell MI, Adhikari S. Magnetopiezoelectric energy harvesting driven by random excitations. *Appl Phys Lett* 2010;96. <https://doi.org/10.1063/1.3436553>.
- [41] Qian F, Hajj MR, Zuo L. Bio-inspired bi-stable piezoelectric harvester for broadband vibration energy harvesting. *Energy Convers Manag* 2020;222. <https://doi.org/10.1016/j.enconman.2020.113174>.
- [42] Taufan I, Nico V, Punch J. Numerical study of a piezoelectric vibration energy harvester without and with an ortho-planar spring using a modified h-shape structure. *Smart Materials, Adaptive Structures and Intelligent Systems* 2023. <https://doi.org/10.1115/SMASIS2023-109903>.
- [43] Rhimi M. Power management and damage assessment techniques for self-powered sensing based on piezoelectric transduction. Ph.D Dissertation. Michigan, USA: 2013.
- [44] Van der Walt M, Crabtree T, Albantow C. PLA as a suitable 3D printing thermoplastic for use in external beam radiotherapy. *Australas Phys Eng Sci Med* 2019;42:1165–76. <https://doi.org/10.1007/s13246-019-00818-6>.
- [45] Aveen KP, Vishwanath Bhajathari F, Jambagi SC. 3D Printing & Mechanical Characterisation of Poly(lactic Acid) and Bronze Filled Poly(lactic Acid) Components. *IOP Conf Ser Mater Sci Eng*, vol. 376, Institute of Physics Publishing; 2018. <https://doi.org/10.1088/1757-899X/376/1/012042>.
- [46] Torun AR, Yıldız EC, Kaya ŞH, Choupani N. Mixed-mode fracture behavior of 3D-printed PLA with zigzag filling. *Green Mater* 2020;9:29–36. <https://doi.org/10.1680/jgrma.20.00013>.
- [47] Comsol. Piezoelectric Energy Harvester. n.d.
- [48] Cottone F. Nonlinear piezoelectric generators for vibration energy harvesting. Ph.D Dissertation. Perugia, Italy: 2007.
- [49] Kim KJ, Cottone F, Goyal S, Punch J. Energy scavenging for energy efficiency in networks and applications. *Bell Labs Tech J* 2010;15:7–29. <https://doi.org/10.1002/bltj.20438>.
- [50] Tang L, Yang Y. A multiple-degree-of-freedom piezoelectric energy harvesting model. *J Intell Mater Syst Struct* 2012;23:1631–47. <https://doi.org/10.1177/1045389X12449920>.
- [51] Cho H, Jeong B, Yu MF, Vakakis AF, McFarland DM, Bergman LA. Nonlinear hardening and softening resonances in micromechanical cantilever-nanotube systems originated from nanoscale geometric nonlinearities. *Int J Solids Struct* 2012;49:2059–65. <https://doi.org/10.1016/j.jisols.2012.04.016>.
- [52] Cottone F, Basset P, Vocca H, Gammaitoni L, Bourouina T. Bistable electromagnetic generator based on buckled beams for vibration energy harvesting. *J Intell Mater Syst Struct*

- 2014;25:1484–95.
<https://doi.org/10.1177/1045389X13508330>.
- [53] Nico V, Frizzell R, Punch J. The Identification of Period Doubling in a Nonlinear Two-Degree-of-Freedom Electromagnetic Vibrational Energy Harvester. *IEEE/ASME Transactions on Mechatronics* 2020;25:2973–80. <https://doi.org/10.1109/TMECH.2020.3000431>.
- [54] Raj A, Steingart D. Review—Power Sources for the Internet of Things. *J Electrochem Soc* 2018;165:B3130–6. <https://doi.org/10.1149/2.0181808jes>.
- [55] Zhang Y, Wang T, Luo A, Hu Y, Li X, Wang F. Micro electrostatic energy harvester with both broad bandwidth and high normalized power density. *Appl Energy* 2018;212:362–71. <https://doi.org/10.1016/j.apenergy.2017.12.053>.
- [56] Aktakka EE, Peterson L. R, Najafi K. A CMOS-Compatible Piezoelectric Vibration Energy Scavenger Based on the Integration of Bulk PZT Films on Silicon. 2010. <https://doi.org/10.1109/IEDM.2010.5703459>.
- [57] Cho KH, Park HY, Heo JS, Priya S. Structure-performance relationships for cantilever-type piezoelectric energy harvesters. *J Appl Phys* 2014;115. <https://doi.org/10.1063/1.4879876>.
- [58] Jiang W, Wang L, Zhao L, Luo G, Yang P, Ning S, et al. Modeling and design of V-shaped piezoelectric vibration energy harvester with stopper for low-frequency broadband and shock excitation. *Sens Actuators A Phys* 2021;317. <https://doi.org/10.1016/j.sna.2020.112458>.
- [59] Pillatsch P, Yeatman EM, Holmes AS. A piezoelectric frequency up-converting energy harvester with rotating proof mass for human body applications. *Sens Actuators A Phys* 2014;206:178–85. <https://doi.org/10.1016/j.sna.2013.10.003>.
- [60] Wu Y, Qiu J, Zhou S, Ji H, Chen Y, Li S. A piezoelectric spring pendulum oscillator used for multi-directional and ultra-low frequency vibration energy harvesting. *Appl Energy* 2018;231:600–14. <https://doi.org/10.1016/j.apenergy.2018.09.082>.
- [61] Magdy MM, El-Bab AMRF, Assal SFM. Design Methodology of a Micro-Scale 2-DOF Energy Harvesting Device for Low Frequency and Wide Bandwidth. *J Sens Technol* 2014;04:37–47. <https://doi.org/10.4236/jst.2014.42005>.
- [62] Gu L. Low-frequency piezoelectric energy harvesting prototype suitable for the MEMS implementation. *Microelectronics J* 2011;42:277–82. <https://doi.org/10.1016/j.mejo.2010.10.007>.
- [63] Xie Z, Huang B, Fan K, Zhou S, Huang W. A magnetically coupled nonlinear T-shaped piezoelectric energy harvester with internal resonance. *Smart Mater Struct* 2019;28. <https://doi.org/10.1088/1361-665X/ab4acb>.
- [64] Challa VR, Prasad MG, Shi Y, Fisher FT. A vibration energy harvesting device with bidirectional resonance frequency tunability. *Smart Mater Struct* 2008;17. <https://doi.org/10.1088/0964-1726/17/01/015035>.
- [65] Adachi K, Tanaka T. An experimental power generation evaluation of cantilever type of piezoelectric vibration energy harvester. *Smart Materials, Adaptive Structures and Intelligent Systems* 2009. <https://doi.org/https://doi.org/10.1115/SMASIS2009-1343>.
- [66] Leland ES, Lai EM, Wright PK. A Self-Powered Wireless Sensor for Indoor Environmental Monitoring. *WNCG Conference, Austin: 2004*.
- [67] Erturk A, Inman DJ. An experimentally validated bimorph cantilever model for piezoelectric energy harvesting from base excitations. *Smart Mater Struct* 2009;18. <https://doi.org/10.1088/0964-1726/18/2/025009>.
- [68] Liu H, Tay CJ, Quan C, Kobayashi T, Lee C. Piezoelectric MEMS energy harvester for low-frequency vibrations with wideband operation range and steadily increased output power. *Journal of Microelectromechanical Systems* 2011;20:1131–42. <https://doi.org/10.1109/JMEMS.2011.2162488>.
- [69] Berdy DF, Srisungsitthisunti P, Jung B, Xu X, Rhoads JF, Peroulis D. Low-frequency meandering piezoelectric vibration energy harvester. *IEEE Trans Ultrason Ferroelectr Freq Control* 2012;59:846–58. <https://doi.org/10.1109/TUFFC.2012.2269>.
- [70] Quintero AV, Besse N, Janphuang P, Lockhart R, Briand D, De Rooij NF. Design optimization of vibration energy harvesters fabricated by lamination of thinned bulk-PZT on polymeric substrates. *Smart Mater Struct* 2014;23. <https://doi.org/10.1088/0964-1726/23/4/045041>.